Chaotic dynamics in quantum-dot miniband superlattices

J. C. Cao
State Key Laboratory of Functional Materials for Informatics, Shanghai Institute of Metallurgy, Chinese Academy of Sciences, 865 Changning Road, Shanghai 200050, People's Republic of China
and Institute for Microstructural Sciences, National Research Council, Ottawa, Ontario, Canada K1A 0R6

H. C. Liu
Institute for Microstructural Sciences, National Research Council, Ottawa, Ontario, Canada K1A 0R6

X. L. Lei
China Center of Advanced Sciences and Technology (World Laboratory), P.O. Box 8730, Beijing 100080, China
and State Key Laboratory of Functional Materials for Informatics, Shanghai Institute of Metallurgy, Chinese Academy of Sciences, 865 Changning Road, Shanghai 200050, People's Republic of China
(Received 3 September 1999)

We have theoretically studied chaotic dynamics of ballistic electrons in GaAs-based quantum dot miniband superlattices under the influence of an intense terahertz electromagnetic radiation, using the balance equations coupling the self-consistent field equation. The electron motion that incorporates the influence of the self-consistent field within the miniband superlattices produces a cooperative nonlinear oscillatory mode, which can lead to complicated chaotic dynamics with the driving amplitude, driving frequency, and the relaxation frequency of the external circuit as the controlling parameters. The temporal behaviors of the solutions of the nonlinear dynamical system are analyzed by using different methods, such as phase portrait, power spectra, first return map, and Lyapunov exponent. The two-dimensional driving amplitude-frequency phase diagrams are calculated with a realistic treatment of scattering contributions by impurity, acoustic phonon, and polar-optic phonons in order to visualize the chaotic regions in the parameter space. The dependence of chaotic regions on the superlattice parameter, lattice temperature, and external circuit condition, is extensively investigated, which provides useful guidance of controlling chaos in realistic device applications.

I. INTRODUCTION

Due to the advance in semiconductor nanostructure fabrication and the development of free-electron laser, the nonlinear dynamics involving electron transport in semiconductor superlattice[1] driven by an intense terahertz (THz) electromagnetic radiation has recently become a central focus of many experimental and theoretical studies.[2–11] Under the influence of external THz electric field, semiconductor superlattices exhibit many interesting phenomena related to negative differential velocity (NDV) in the stationary current-voltage characteristic. It was reported that the current through a dc-biased GaAs/AlAs superlattice miniband is reduced when the system is exposed to an intense ac field having a frequency from about 0.1 (Refs. 12–14) to several[9,11] THz. Moreover, when a superlattice is driven by a strong high-frequency electric field, abundant harmonics may generate, and thus it is considered useful as a broad band source of THz radiation.[10,11] Recently, by involving novel electromagnetic radiation sources and coupling techniques the effect of THz radiation field on the nonlinear current-voltage characteristics of miniband superlattices has been investigated experimentally, including multiphoton-assisted resonant tunneling,[6] negative absolute resistance,[7] and Shapiro steps on dc current-voltage curve.[8] Also, it is noted that when a miniband superlattice[14,15] or a sequential resonant tunneling superlattice[16–19] is subjected to a dc+ac field the superlattice system can produce an alternative mode of operation and lead to the transition between the synchronized current oscillation and various types of deterministic spatiotemporal chaos. The bifurcation scenario to chaos for electron transport was further studied experimentally in an incommensurately driven superlattice system.[20]

Theoretically, interaction of semiconductor superlattice with an intense electromagnetic radiation can be simulated[2–5,14–17] as the response of a biased or unbiased superlattice to a large-amplitude high-frequency sinusoidal/cosinoidal field. For superlattice miniband transport the earliest model of Esaki and Tsu,[1] considering a single electron moving in an one-dimensional miniband with a constant scattering time, gave a simple relation between the drift velocity and the electric field. The another is the balance-equation theory developed for miniband superlattice transport in semiconductor superlattice[21–23] with realistic impurity scattering and electron-phonon interactions, predicting a widely varying temperature and miniband-width-dependent velocity-field behavior. Recently, Alekseev *et al.*[4,5] studied the influence of an intense THz electric field on the motion of ballistic electrons in a miniband superlattice using a set of phenomenological balance equations coupling the self-consistent field equation within the relaxation time approximations. They showed that accounting for collective effects (via a self-consistent field) leads to the possibility of chaotic dynamics, and investigated the dependence of chaotic dynamics on the relaxation times. The method[4,5] is similar with the Esaki-Tsu-type approach. However, the phenom-

enological elastic and inelastic scattering times introduced in the constant-relaxation-time approximation[4,5] are difficult to estimate from the electron-impurity and electron-phonon coupling information of the materials. There is a clear need to understand the extent to which the phenomenological balance-equation approach correctly captures the realistic superlattice physics. The balance-equation theory[21–23] may be a good candidate for doing this since the realistic energy-dispersion relation and all realistic electron-impurity and electron-phonon scatterings are taken into full account from the material information of the superlattice on the microscopic level.

The purpose of this paper is to present a careful study of chaotic dynamics of quantum-dot miniband superlattice driven by an intense THz radiation field based on the balance equations[21–23] coupling the influence of the self-consistent field.[4,5] We provide a method for studying chaotic dynamics in miniband superlattice by considering detailed superlattice physics without invoking the constant relaxation-time approximation. In contrast with the work by Alekseev *et al.*,[4,5] here we yield the energy-dependent momentum- and energy-relaxation times from the microscopic frictional acceleration and energy-transfer rate functions with an accurate treatment of impurity, acoustic phonon (interacting with electrons through deformation and piezoelectric potentials), and polar-optic scatterings. This allows us to obtain self-consistently the dependence of chaotic dynamics on the superlattice parameter and lattice temperature.

The remainder of this paper is organized as follows. In Sec. II, we describe the time-dependent momentum- and energy-balance equations for a quantum-dot miniband superlattice under the influence of an electric field and outline the derivation of the self-consistent field equation from Kirchoff's theorem. In Sec. III, we calculate the steady-state velocity-field relations showing the NDV, and determine the energy-dependent momentum- and energy-relaxation times from the frictional acceleration and energy-loss rate functions. The chaotic dynamics are studied in detail by several different methods for detecting chaotic characteristics of a time series in Sec. IV. In Sec. V, the dependence of the chaotic regions on the superlattice parameter, lattice temperature, and the relaxation frequency of the external circuit has been extensively investigated by performing a large number of calculations for different quantum dot superlattices at different lattice temperatures. In Sec. VI, we draw the main conclusions and remarks on the differences and connections between the present work and other recent publications.

II. BALANCE EQUATIONS FOR QUANTUM DOT MINIBAND SUPERLATTICES

Consider a superlattice along the z direction, which is formed by periodical potential wells and barriers of finite height. In the xy plane there exists an infinitely high-potential wall such that electrons are confined in a small cylindrical region of diameter d_r. The single-electron state of the system can be described by transverse quantum numbers, a longitudinal miniband index and a longitudinal wave vector k_z ($-\pi/d<k_z\leqslant\pi/d$, where d is the period of the superlattice). We assume that the energy separation between the transverse ground and excited states, and the energy gap between the longitudinal lowest and second minibands, are large enough, then only the transverse ground state and the longitudinal lowest miniband need be taken into consideration. We thus have a quasi-one-dimensional system, the state of which can be described by a one-dimensional wave vector k_z, with the energy dispersion, under the tight-binding approximation, expressed in the form

$$\varepsilon(k_z)=\frac{\Delta}{2}[1-\cos(k_z d)], \tag{1}$$

where Δ is the miniband width. When an external ac electric field with amplitude E_Ω and frequency Ω,

$$E_{\rm ext}(t)=E_\Omega\cos(\Omega t), \tag{2}$$

is applied in the superlattice direction, i.e., in the motion direction of electrons within the superlattice miniband. The self-consists field $E_{\rm sc}$ is related to the voltage U across the superlattice by $E_{\rm sc}=U/l$ with l the length of the superlattice. The total current density J through the superlattice consists of two parts: the displacement current $j_{\rm disp}=\epsilon_s dE_{\rm sc}/dt$ (here, ϵ_s is the average dielectric constant for the superlattice) and the current of ballistic electrons $j=-env_d$, where e is the carrier charge, n is the bulk density of carriers, and v_d is the electron velocity. Kirchoff's equation for the resistively shunted superlattice[5] is $(\epsilon_s dE_{\rm sc}/dt-env_d)S+E_{\rm sc}l/R=0$, i.e.,

$$\frac{dE_{\rm sc}}{dt}=-\frac{env_d}{\epsilon_s}-\Lambda E_{\rm sc}, \tag{3}$$

which provides the circuit contribution to the damping of the self-consistent field generated by the electron current in the superlattice. In Eq. (3), $\Lambda=(RC)^{-1}$ is the relaxation frequency of the external circuit, R is the resistance of the external circuit, and $C=\epsilon_s S/l$ is the superlattice capacitance with S the cross area of the superlattice.

The electric field acting on the electrons, $F(t)$, is the sum of the external ac field $E_{\rm ext}(t)$ and the self-consistent field $E_{\rm sc}(t)$, which incorporates the influence of the circuit and of the repulsive interaction with other electrons on a single electron's dynamics,[5] i.e., $F(t)=E_{\rm sc}(t)+E_{\rm ext}(t)$. According to the balance-equation theory,[22] under the influence of electric field F, the carriers in the superlattice are accelerated by the field and scattered by impurities and by phonons, resulting in an overall drift motion and possible heating of the carrier system. Such a transport state of the system is described by the center-of-mass momentum $P_d=Np_d$ (N is the total number of carriers) and the relative electron temperature T_e, and they are determined by the effective force- and energy-balance equations,[21–23]

$$\frac{dv_d}{dt}=eF/m_z^*+A, \tag{4}$$

$$\frac{dh_e}{dt}=eFv_d-W, \tag{5}$$

in which,

$$v_d=\frac{2}{N}\sum_{k_z} v(k_z)f[\overline{\varepsilon}(k_z),T_e], \tag{6}$$

is the average drift velocity of the electrons with $v(k_z)=d\varepsilon(k_z)/dk_z$ the velocity function in the z direction,

$$h_e=\frac{2}{N}\sum_{k_z} \varepsilon(k_z)f[\overline{\varepsilon}(k_z),T_e], \tag{7}$$

is the average electron energy, and

$$\frac{1}{m_z^*}=\frac{2}{N}\sum_{k_z}\frac{1}{\hbar^2}\frac{d^2\varepsilon(k_z)}{dk_z^2}f[\overline{\varepsilon}(k_z),T_e], \tag{8}$$

is an ensemble-averaged inverse effective mass, introduced to describe the response of the electron system to an external field. In these expressions, $f[\overline{\varepsilon}(k_z),T_e]=1/\exp(\{[\overline{\varepsilon}(k_z)-\mu]/k_BT_e\}+1)$ is the Fermi distribution function at the electron temperature T_e, μ is the chemical potential determined by the condition

$$N=2\sum_{k_z} f[\overline{\varepsilon}(k_z),T_e], \tag{9}$$

and

$$\overline{\varepsilon}(k_z)=\varepsilon(k_z-p_d/\hbar), \tag{10}$$

is the relative electron energy. In Eqs. (4) and (5) A is frictional acceleration consisting of the impurity- and phonon-induced frictional accelerations, A_i and A_p, and W is the energy-transfer rate from the electron system to the phonon system. They share the same expressions as those given in Ref. 22, which are completely determined by p_d, T_e, and μ for a quantum dot miniband superlattice with the known confined structure, impurity distributions, phonon modes, electron-impurity potentials, and electron-phonon coupling matrix elements.

With the miniband energy dispersion relation expressed by Eq. (1), the electron density per unit length along the z direction N_1 for the determination of the chemical potential μ can be written as[22]

$$N_1d=\frac{1}{\pi}\int_{-\pi}^{\pi}\frac{dz}{\exp\{[(\Delta/2)(1-\cos z)-\mu]/k_BT_e\}+1}. \tag{11}$$

The average drift velocity, the inverse effective mass, and the average energy of the system can be respectively expressed as

$$v_d=v_m\alpha_1(T_e)\sin\left(\frac{p_dd}{\hbar}\right), \tag{12}$$

$$\frac{1}{m_z^*}=\frac{1}{M^*}\alpha_1(T_e)\cos\left(\frac{p_dd}{\hbar}\right), \tag{13}$$

$$h_e=\frac{\Delta}{2}\left[1-\alpha_1(T_e)\cos\left(\frac{p_dd}{\hbar}\right)\right], \tag{14}$$

with $v_m=\Delta d/(2\hbar)$, $M^*=2\hbar^2/(\Delta d^2)$, and

$$\alpha_1(T_e)=\frac{1}{\pi N_1d}\int_{-\pi}^{\pi}\frac{\cos z\,dz}{\exp\{[(\Delta/2)(1-\cos z)-\mu]/k_BT_e\}+1}$$
$$=\frac{\int_{-\pi}^{\pi}\frac{\cos z\,dz}{\exp\{[(\Delta/2)(1-\cos z)-\mu]/k_BT_e\}+1}}{\int_{-\pi}^{\pi}\frac{dz}{\exp\{[(\Delta/2)(1-\cos z)-\mu]/k_BT_e\}+1}}. \tag{15}$$

The thermal-equilibrium energy is $h_{e0}=\Delta/2[1-\alpha_1(T)]$ with T the lattice temperature. In the Boltzmann's distribution limit (under the condition of a small carrier density and a high temperature), we have $\alpha_1(T_e)=I_1[\Delta/(2k_BT_e)]/I_0[\Delta/(2k_BT_e)]$ with $I_1(x)=1/\pi\int_0^{\pi}\cos\theta\exp(x\cos\theta)d\theta$ and $I_0(x)=1/\pi\int_0^{\pi}\exp(x\cos\theta)d\theta$ the modified Bessel functions. k_B is Boltzmann's constant.

In terms of physical meaning of p_d we assume $p_dd/\hbar\in[0,\pi]$, then Eqs. (12) and (14) determine one 1 to 1 map g from point (p_d,T_e) to (v_d,h_e), i.e., $(v_d,h_e)=g(p_d,T_e)$, and its inverse map g^{-1} exists, which we define by $(p_d,T_e)=g^{-1}(v_d,h_e)$, so for given (v_d,h_e) we can obtain the only (p_d,T_e) from Eqs. (12) and (14). Therefore, according to definitions of A and W, we can define the momentum- and energy-relaxation frequencies, respectively, by

$$\nu_{1v}\equiv-\frac{A(p_d,T_e)}{v_d}=-\frac{A[g^{-1}(v_d,h_e)]}{v_d}, \tag{16}$$

$$\nu_{1\varepsilon}\equiv\frac{W(p_d,T_e)}{h_e-h_{e0}}=\frac{W[g^{-1}(v_d,h_e)]}{h_e-h_{e0}}. \tag{17}$$

For the calculations that follow, it is convenient to render the equations dimensionless. We set the scaling factors as follows: velocity $v_s=v_m$, energy $h_s=\Delta/2$, mass $m_s=M^*$, frequency $\omega_s=\sqrt{e^2n/(\epsilon_sM^*)}$, time $t_s=1/\omega_s$, electric field $E_s=\hbar\omega_s/(ed)$, electron temperature $T_s=h_s/k_B$, momentum $p_s=\hbar/d$, acceleration $A_s=v_s/t_s$, and energy-transfer rate $W_s=h_s/t_s$. The dimensionless quantities are denoted by: electric field $E=F/E_s$, ac amplitude $E_\omega=E_\Omega/E_s$, velocity $v=v_d/v_s$, energy $\varepsilon=h_e/h_s$, thermal equilibrium energy $\varepsilon_0=h_{e0}/h_s$, time $\tau=t/t_s$, ac frequency $\omega=\Omega/\omega_s$, circuit relaxation frequency $\alpha=\Lambda/\omega_s$, momentum- and energy-relaxation frequencies $\nu_{v,\varepsilon}=\nu_{1v,1\varepsilon}/\omega_s$, acceleration $\tilde{A}=A/A_s$, and energy-transfer rate $\tilde{W}=W/W_s$. Then, we obtain the dimensionless equations of Eqs. (3)–(5) as follows

$$\frac{dv}{d\tau}=(1-\varepsilon)E-\nu_vv, \tag{18}$$

$$\frac{d\varepsilon}{d\tau}=Ev-\nu_\varepsilon(\varepsilon-\varepsilon_0), \tag{19}$$

$$\frac{dE}{d\tau}=-v-\alpha E+f(\tau), \tag{20}$$

in which $f(\tau)=\alpha E_\omega\cos(\omega\tau)-E_\omega\omega\sin(\omega\tau)$, ν_v and ν_ε are calculated from the dimensionless version of Eqs. (16) and (17), i.e.,

$$\nu_v = -\frac{\tilde{A}(v,\varepsilon)}{v}, \tag{21}$$

$$\nu_\varepsilon = \frac{\tilde{W}(v,\varepsilon)}{\varepsilon - \varepsilon_0}. \tag{22}$$

Now, we have three ordinary differential equations, (18), (19), and (20), which describe the motion of the electrons in the miniband superlattice under the influence of the external THz field, $E_\omega \cos(\omega\tau)$, and internal self-consistent field. These equations have the same forms with those given by Alekseev *et al.* in Ref. 4. The most important difference between them is the input of ν_v and ν_ε. In the present balance equations ν_v and ν_ε are given, respectively, by the microscopic frictional acceleration $\tilde{A}$ and energy-transfer rate functions $\tilde{W}$, which are completely determined by the energy-wave-vector dispersion and scattering constants of materials, while in the Alekseev's model ν_v and ν_ε are simply two phenomenological constants unrelated to the equations and the material itself. For solving Eqs. (18)–(20), we set the initial conditions as $v(0)=0$, $\varepsilon(0)=\varepsilon_0$, and $E(0)=E_\omega$, which correspond to the initially unexcited superlattice just being struck by the incident electromagnetic radiation field. For the numerics we use the integrating-one-step Gill algorithm incorporating adaptive step size, convergence checking with an accuracy of 10^{-6}, and offset of accumulation error.

III. STEADY-STATE VELOCITY-FIELD RELATIONS AND DETERMINATION OF ENERGY-DEPENDENT RELAXATION FREQUENCIES

To recall how we calculate the frictional acceleration $\tilde{A}$ and energy-transfer rate $\tilde{W}$, as an example, we have calculated the steady-state drift velocity as a function of the electric field E from the steady-state version of the balance Eqs. tions (18) and (19) for a GaAs-based quantum-dot miniband superlattice. Throughout the paper we assume the superlattice period $d=15$ nm, well width $a=10$ nm, transverse diameter $d_r=10$ nm, low-temperature (4.2 K) linear mobility $\mu_0=0.1$ m^2/V s, and the carrier sheet density of $N_s=1.6\times10^{12}$ cm^{-2} (per period) in the transverse plane, corresponding to a bulk density $n=N_s/d=1.07\times10^{18}$ cm^{-3} or a line density $N_1 d=\pi(d_r/2)^2 N_s=1.257$. Scatterings due to charged impurities, acoustic phonons (interacting with electrons through deformation and piezoelectric potentials), and optic phonons are taken into account in the calculations. All the material constants used here are typical values of bulk GaAs: mass density 5.31 g/cm^3, electron-band-effective cross mass $m=0.067m_e$ (m_e is the free electron mass), transverse sound velocity $v_{st}=2.48\times10^3$ m/s, longitudinal sound velocity $v_{sl}=5.29\times10^3$ m/s, LO phonon energy $\Omega_{\rm LO}=35.4$ meV, low-frequency dielectric constant $\kappa=12.9$, optical dielectric constant $\kappa_\infty=10.8$, acoustic deformation potential $\Xi=8.5$ eV, and piezoelectric constant $e_{14}=1.41\times10^9$ V/m. From these given material and superlattice structural parameters, $\tilde{A}$ and $\tilde{W}$ is completely determined as functions of p_d and T_e [see Eqs. (10)–(12) in Ref. 22]. In Fig. 1 we show the calculated drift velocity v (in unit of v_s)

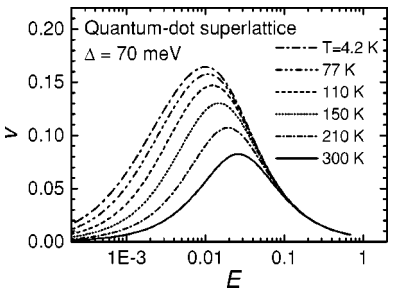

FIG. 1. Velocity-field relations calculated from the steady-state version of the balance Eqs. (18) and (19) with a self-consistent treatment of the frictional acceleration $\tilde{A}$ and energy-transfer rate $\tilde{W}$ for the quantum-dot miniband superlattice of $\Delta=70$ meV at different lattice temperatures: $T=4.2, 77, 110, 150, 210,$ and 300 K, respectively. The parameters: superlattice period $d=15$ nm, well width $a=10$ nm, transverse diameter $d_r=10$ nm, electron sheet density $N_s=1.6\times10^{12}$ cm^{-2}, and low-temperature (4.2 K) linear mobility $\mu_0=0.1$ m^2/V s, are maintained unchanged throughout the paper.

as a function of the steady-state electric field E (in unit of E_s) for the superlattice of $\Delta=70$ meV at lattice temperatures $T=4.2, 77, 110, 150, 210,$ and 300 K, respectively. They obviously show a varying temperature-dependent negative-differential-velocity behavior.

In the recent work by Alekseev *et al.*,[4,5] phenomenological constant relaxation frequencies ν_v and ν_ε are assumed to study nonlinear dynamics of the miniband superlattice system driven by a THz electric field. In real superlattices, however, the relaxation frequencies largely depend on microscopic scattering mechanics and superlattice parameters. The present balance-equation formulas allow one self-consistently determining this dependence from Eqs. (21) and (22) as follows. Let $p_d d/\hbar \in (0,\pi)$, and set the changing range of the electron temperature to be: $T_e/T \in (1,160)$, which are wide enough for hot-electron regime of the superlattice system considered here. Then, with changing p_d and T_e arbitrary in the setting range we simultaneously calculate ν_v, ν_ε, and ε as functions of p_d and T_e, respectively, from Eqs. (21) and (22), and the dimensionless energy $\varepsilon=1-\alpha_1(T_e)\cos(p_d d/\hbar)$ scaled from Eq. (14). In Fig. 2, we show

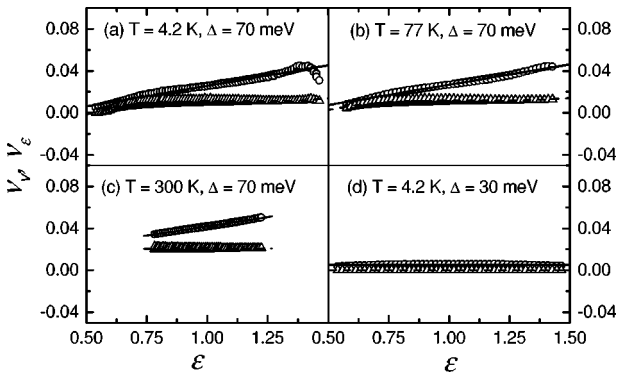

FIG. 2. Calculated energy-dependent momentum-relaxation frequencies ν_v (open circles) and energy-relaxation frequencies ν_ε (open triangles) for the quantum dot miniband superlattices of $\Delta=30$ and 70 meV at different lattice temperatures: $T=4.2$, 77, and 300 K, respectively. The lines are the numerically-fitted results.

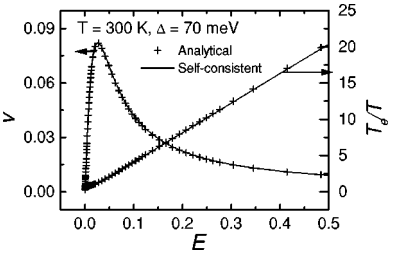

FIG. 3. Steady-state electron velocities and electron temperatures as functions of the electric field for the quantum dot miniband superlattice of $\Delta=70$ meV at $T=300$ K, respectively, calculated from the original $\tilde{A}$ and $\tilde{W}$ (lines) and by the numerically-fitted formula (25) (open circles) of ν_v and ν_ε.

ν_v (open circles) and ν_ε (open uptriangles) as a function of energy ε calculated from Eqs. (21) and (22) for the quantum dot superlattices of miniband width $\Delta=30$ and 70 meV at lattice temperatures $T=4.2$, 77, and 300 K, respectively. The lines in Fig. 2 are the numerically fitted energy-dependent ν_v (solid line) and energy-dependent ν_ε (dashed line) by following expressions,

$$\nu_v=-0.01349+0.03919\varepsilon,$$

$$\nu_\varepsilon=-0.06645+0.21047\varepsilon-0.18995\varepsilon^2+0.05691\varepsilon^3,$$

$$\text{when}\quad \Delta=70\ \text{meV},\quad T=4.2\ \text{K}, \tag{23}$$

$$\nu_v=-0.01212+0.0389\varepsilon,$$

$$\nu_\varepsilon=-0.04324+0.15058\varepsilon-0.13752\varepsilon^2+0.04178\varepsilon^3,$$

$$\text{when}\quad \Delta=70\ \text{meV},\quad T=77\ \text{K}, \tag{24}$$

$$\nu_v=0.00651+0.03533\varepsilon,$$

$$\nu_\varepsilon=0.02009,\quad \text{when}\quad \Delta=70\ \text{meV},\quad T=300\ \text{K}, \tag{25}$$

$$\nu_v=0.00488,\quad \nu_\varepsilon=1.85341\times10^{-4},$$

$$\text{when}\quad \Delta=30\ \text{meV},\quad T=4.2\ \text{K}. \tag{26}$$

The fitting processes are completed by Polynomial Regression with the standard deviations less than 10^{-4}. As a check of the accuracy of the analytical expressions, we show in Fig. 3 the steady-state electron velocity and electron temperature as a function of electric field E at $\Delta=70$ meV and $T=300$ K, calculated, respectively, from the original $\tilde{A}$ and $\tilde{W}$ (lines) and from the numerically-fitted formulas (25) (pluses). A good agreement is found between the two results in the full range of the electric field.

Specially, when relaxation frequencies ν_v and ν_ε are both constant as the case of $\Delta=30$ meV and $T=4.2$ K showed in Eq. (26), a straightforward calculation from the steady-state version of Eqs. (18) and (19) yields the dimensionless dc velocity-field relation,

$$v=2v_p\frac{E/E_c}{1+(E/E_c)^2}, \tag{27}$$

with the critical electric field, $E_c=\sqrt{\nu_v\nu_\varepsilon}$, at which the dc drift velocity peaks, and peak velocity $v_p=\sqrt{\nu_\varepsilon/\nu_v}/2\cdot\alpha_1(T)$, so in the regime of $E>E_c$ there is a negative differential velocity. Also, we obtain the zero-frequency dc mobility for the electric field E as

$$\mu_c\equiv\frac{v}{E}=\frac{E\nu_\varepsilon\alpha_1(T)}{E^2+\nu_v\nu_\varepsilon}, \tag{28}$$

and the zero-frequency differential mobility as

$$\mu_0\equiv\frac{dv}{dE}=\frac{(E^2-\nu_v\nu_\varepsilon)\nu_\varepsilon\alpha_1(T)}{(E^2+\nu_v\nu_\varepsilon)^2}. \tag{29}$$

It is obvious that Eq. (27) reduces to the Alekseev's result [see Eq. (6) in Ref. 4] in the Boltzmann limit {so $\alpha_1(T)=I_1[\Delta/(2k_BT)]/I_0[\Delta/(2k_BT)]$}, and furthermore reduces to the original Esaki-Tsu's result in the zero-temperature limit [so $\alpha_1(T)\equiv1$] and when we choose $\nu_v=\nu_\varepsilon=1/\tau_0$ with τ_0 the scattering time. In this regard, it is worth noting that the generalization of the formula of Esaki and Tsu to finite temperature and to the case of $\nu_v\neq\nu_w$ describes with reasonable accuracy the steady-state transport properties of the miniband electrons in the Fermi distribution.

IV. CHAOTIC DYNAMICS IN THE PRESENCE OF A THz FIELD

To study the chaotic dynamics from Eqs. (18), (19), and (20), we need solve three independent variables: velocity v, energy ε, and electric field E, involving three controlling parameters: ac amplitude E_ω, ac frequency ω, and circuit relaxation frequency α. In principle, we can directly solve Eqs. (18)–(20) with a self-consistent treatment of $\tilde{A}$ and $\tilde{W}$ appearing in Eqs. (21) and (22). However, to do it like this is very time consuming, thus preventing us from an extensive investigation on different superlattice parameters and lattice temperatures, because $\tilde{A}$ and $\tilde{W}$ are in the form of multilayered integrals.[22] On the other hand, the accuracy of multilayered numerically-integrating may lead some uncertainty of the obtained results since the solution of a nonlinear dynamical system is very sensitive to the numerics employed, so we instead use the numerically fitted energy-dependent momentum- and energy-relaxation frequencies ν_v and ν_ε given by Eqs. (23)–(26) to explore the chaotic dynamics in quantum-dot miniband superlattices. Since the average electron velocity v is the variable most directly related to experimental observable, we study the temporal behavior of the superlattice system from the electron velocity. By directly solving Eqs. (18)–(20) subject to different external ac electric fields, we have found different temporal behavior of the solutions of the miniband superlattice system, depending upon the amplitude E_ω and frequency ω of the ac field. The behavior of the solutions observed in our calculations can be referred to the following three types: periodic, chaotic, and quasiperiodic, which are the typical modes commonly appearing in different nonlinear dynamical systems.[24] The ''periodic'' behavior means that the electron velocity varies periodically with just the fundamental frequency or its subharmonics of the external ac field. The synchronized oscillation of the electron velocity with the external ac field is

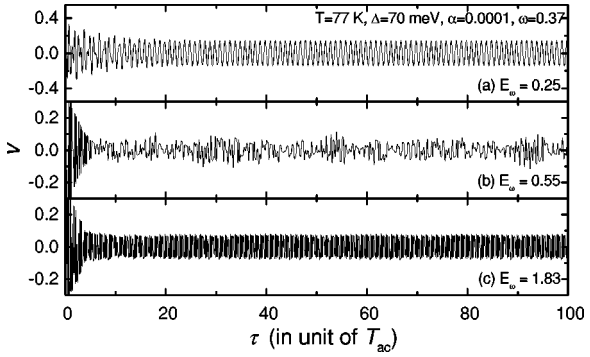

FIG. 4. Time-dependent electron drift velocities for the quantum-dot miniband superlattice of $\Delta=70$ meV at $T=77$ K, $\alpha=0.0001$, $\omega=0.37$, and different ac amplitudes: (a) $E_\omega=0.25$, (b) 0.55, and (c) 1.83, which respectively correspond to the periodic, chaotic, and quasiperiodic solutions.

referred to as ''1:1'' frequency-locking mode; for the ''chaotic'' behavior, the velocity varies erratically and with no apparent periodicity for as long as we observe it, and it is the behavior in which we are most interested; while the ''quasiperiodic'' behavior is somewhat similar either with the ''periodic'' or with the ''chaotic'' states, which are also often encountered in simulations of nonlinear dynamical systems, and can be accurately defined by first return map of the time series (see the following). Figure 4 shows the velocity v vs time τ for ac frequency $\omega=0.37$ and different ac amplitudes: $E_\omega=0.25$, 0.55, and 1.83, which respectively corresponds periodic, chaotic, and quasiperiodic solutions for the quantum-dot superlattice of miniband width $\Delta=70$ meV at lattice temperature $T=77$ K and the circuit relaxation frequency $\alpha=0.0001$. To have an overview of the nonlinear dynamical properties of the superlattice system, in the following subsections we analyze the behavior of the solutions for different controlling parameters, by using several different methods, such as phase portrait, power spectrum analysis, first return map, and Lyapunov exponent, which are often used in detecting the chaotic characteristics of a nonlinear dynamical system.

A. Lyapunov exponent and Poincaré bifurcation diagram

Lyapunov exponents have proven to be the most useful dynamical diagnostic tool for a chaotic system, which are obtained from the average exponential rates of divergence or convergence of nearby orbits in phase space. Any system containing at least one positive Lyapunov exponent is defined to be chaotic. For the chaotic case of $E_\omega=0.55$ described in Fig. 4(b), we have calculated the first three Lyapunov exponents λ_1, λ_2, and λ_3 by using the standard method and computational programs developed[25] for an ordinary differential equation system. In the calculations, the time interval used to average Lyapunov exponent is $\tau_m=mT_{\rm ac}$ with $T_{\rm ac}=2\pi/\omega$ the driving period of the ac field, and the maximal time delay, which we calculate is set to be $175T_{\rm ac}$. The temporal convergencies $\lambda_1(\tau_m)$, $\lambda_2(\tau_m)$, and $\lambda_3(\tau_m)$ of the first three Lyapunov exponents $\lambda_{1,2,3}$ $[\equiv\lim_{m\to\infty}\lambda_{1,2,3}(\tau_m)]$ are shown in Fig. 5. The asymptotic value of the maximal Lyapunov exponent $\lambda_1(\tau_m)$ for the chaotic case of $E_\omega=0.55$ is greater than zero (about

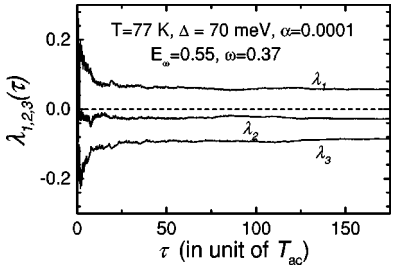

FIG. 5. Temporal convergences of the first three Lyapunov exponents λ_1, λ_2, and λ_3 for the chaotic case of $E_\omega=1.83$ as described in Fig. 4(b).

0.6), as it should be. Following that, we study the same superlattice system as described in Fig. 4 by changing the ac amplitude E_ω, to clarify the periodic regions and the aperiodic (quasiperiodic or chaotic) regions in the parameter space of E_ω. For this purpose, we require the help of Poincaré bifurcation diagram, thus needing to define Poincaré mapping. We adopt the velocities at times $\tau_m=mT_{\rm ac}$, $m=1,2,3,\ldots$, (after the transients die out) as the Poincaré mappings of E_ω. For each E_ω, if the solution $v_m=v(\tau_m)$ is aperiodic, we eliminate the first 100 transient points and depict the next 250 points of v_m as the mappings of E_ω. Otherwise we compute v_m until the solution becomes periodic within an accuracy of 10^{-4}, and depict all the v_m as the mappings of E_ω. In the calculations, the parameter E_ω is changed from 0.1 to 2.0. The calculated Poincaré bifurcation diagram is shown in Fig. 6(a), and the corresponding first three Lyapunov exponents λ_1, λ_2, and λ_3 as functions of E_ω are shown in Fig. 6(b) for the superlattice of $\Delta=70$ meV at $\omega=0.37$, $T=77$ K, and $\alpha=0.0001$. The Poincaré bifurcation diagram indicates that the bifurcation scenario is quite complex, rather than a simple period-doubling cascade commonly appearing in nonlinear dynamical systems. The transition between periodic and aperiodic states changes discontinuously with the parameter E_ω. Even in the periodic region the bifurcation diagram can be discontinue, such as in the region of $E_\omega\in(0.9,1.1)$. For small ac amplitudes $E_\omega<0.3$ the solutions are ''1:1'' frequency-locking. As E_ω in-

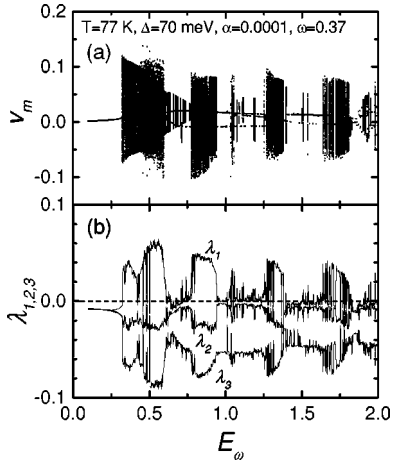

FIG. 6. (a) Poincaré bifurcation diagram and (b) the first three Lyapunov exponents λ_1, λ_2, and λ_3 for the quantum-dot miniband superlattice of $\Delta=70$ meV at $T=77$ K, $\alpha=0.0001$, and $\omega=0.37$.

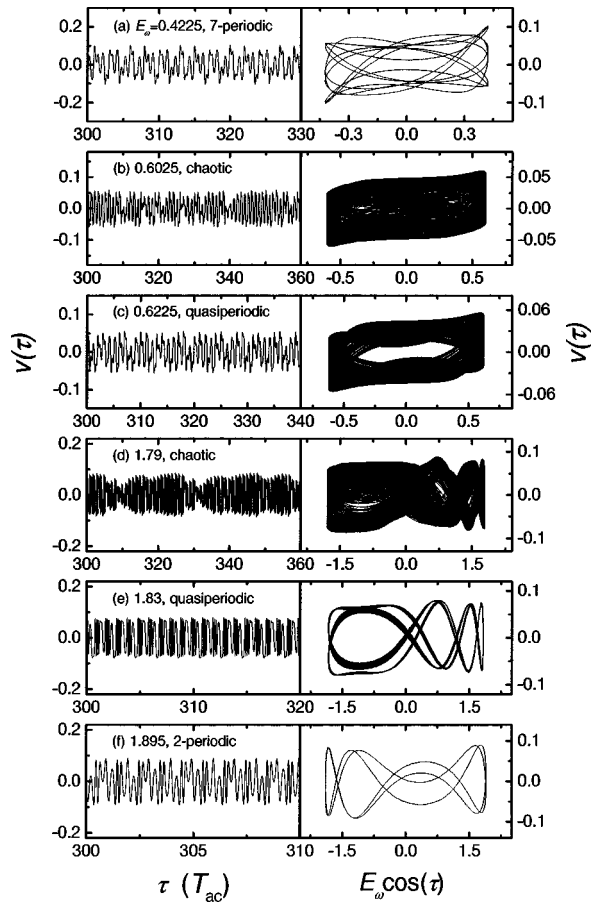

FIG. 7. Time-dependent electron velocities $v(\tau)$ (left) and the corresponding velocity-field phase plots (right) for the six specific driving amplitudes: (a) $E_\omega=0.4225$, (b) 0.6025, (c) 0.6225, (d) 1.79, (e) 1.83, and (f) 1.895, for the quantum dot miniband superlattice described in Fig. 6. Periodic: (a) and (f), quasiperiodic: (c) and (e), and chaotic: (b) and (d).

creases, the frequency-locking solutions with period 2 and 3 etc. are observed, and the transitions from the periodic to aperiodic windows occur over a very small range of E_ω. From the Lyapunov exponents shown in Fig. 6(b) we can clarify the chaotic and quasiperiodic solutions, both having a large number of points in the bifurcation diagram. For the chaotic solutions $\lambda_1>0$, which indicates exponential divergence of nearby trajectories; for the quasiperiodic solutions $\lambda_1=0$ when $\tau\rightarrow\infty$; while for the periodic solutions $\lambda_1<0$. In general, the bifurcation diagram structures shown in Fig. 6(a) for the quantum dot miniband superlattice driven by a THz field are quite different from those for the miniband superlattice driven by a GHz field, which are related to the formation and travelling of electric-field domain.[14]

B. Evolution of solution and velocity-field phase plot

To have a more deeper insight into the time-dependent behavior of the solutions of the miniband superlattice described in Fig. 6, we study in detail six specific cases of the ac amplitudes: (a) $E_\omega=0.4225$, (b) 0.6025, (c) 0.6225, (d) 1.79, (e) 1.83, and (f) 1.895, respectively. In Fig. 7 we plot the time-dependent velocity $v(\tau)$ and the corresponding velocity-field phase plots for the six specific values of E_ω. From the velocity evolutions $v(\tau)$ (the left of Fig. 7), we can clarify periodic and aperiodic solutions, but only from $v(\tau)$-τ relation it is difficult to distinguish a quasiperiodic and chaotic solution from the aperiodic solutions. However, this can be done with the help of the phase plot and first return maps. Experimentally, the velocity-field phase plot could be measured by depicting the electron velocity as a function of the instantaneous value of external electric field. Phase plots for the period solutions appear as simple closed loops [Figs. 7(a) and 7(f)], those for the quasiperiod solutions look more complicated [Figs. 7(c) and 7(e)], while phase plots for the chaotic solutions become very much folder and irregular [Figs. 7(b) and 7(d)]. The Poincaré mappings used to obtain the bifurcation diagram of Fig. 6(a) can be understood from the phase plots (the right of Fig. 7) as the successive crossing points of the orbit through the vertical line $E_\omega\cos(\omega\tau)\equiv E_\omega$, corresponding to the times $\tau=mT_{\rm ac}=2\pi m$. For n-periodic solution the number of the crossing points are just n, while for aperiodic solutions those crossing points are distributed over some interval (or intervals) of the velocity.

C. First return map and Fourier spectrum

By sampling the electron velocity at times $\tau_m=mT_{ac}$, one obtains the data set $v_m=v(mT_{ac})$. The first return map is obtained by plotting v_{m+1} as a function of v_m (here, m is large enough such that the transient state dies out). In the left of Fig. 8 we show the first return maps for the six specific E_ω as described in Fig. 7. It is indicated that the resultant attractors for n-periodic solutions are just the n separate points [see Figs. 8(a) and 8(f)], those for quasiperiodic solutions are simple close curves with a regular distribution of the points [see Figs. 8(c) and 8(e)], while the chaotic attractors contain infinite random points (when $m\rightarrow\infty$), forming several separate branches and a multilayered structure with varying density of the points on different regions [Figs. 8(b) and 8(d)].

Power spectrum analysis is usually considered as an additional effective method to detect chaos. We have calculated by using a fast Fourier transform algorithm and shown power spectra $P(f)$ (arbitrary unit) in the right of Fig. 8 for the six specific values of E_ω as described in Fig. 7. It can be seen that the power spectra for the periodic solutions [Figs. 8(a) and 8(f)] are smooth and have few peaks, corresponding to the driving frequency $f_{\rm ac}$ and its harmonics, those for the quasiperiodic solutions [Figs. 8(c) and 8(e)] are relatively complex, while for the chaotic solutions [Figs. 8(b) and 8(d)] the power spectra become very irregular with a large number of peaks.

V. DEPENDENCE OF CHAOTIC REGIONS ON CONTROLLING PARAMETERS

The best overview of the behavior of the solutions of the superlattice system, chaotic vs periodic, is provided by a two-dimensional phase diagram showing the distribution of chaotic regions where all the maximal Lyapunov exponents are positive as functions of the controlling parameters, driving amplitude E_ω and driving frequency ω. This kind of amplitude-frequency phase diagram can give us a clear visual presentation of the chaotic regions, and has been used

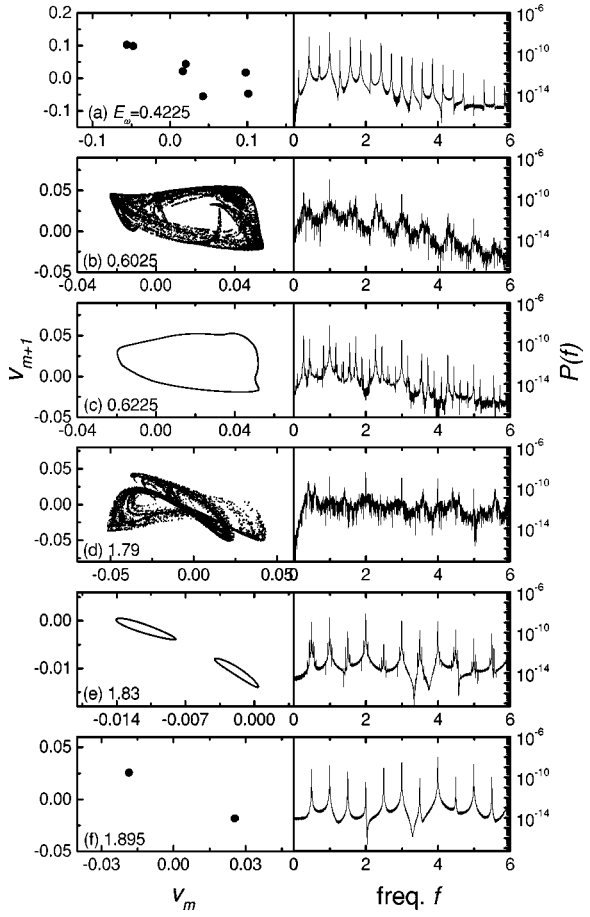

FIG. 8. First return maps (left) and the corresponding power spectra (right) for the six specific driving amplitudes described in Fig. 7. Periodic: (a) and (f), quasiperiodic: (c) and (e), and chaotic: (b) and (d).

very effectively in studies of chaos in nonlinear dynamical systems. The two-dimensional E_ω-ω phase diagrams in this work are obtained as follows: for each E_ω we change ω with a step $\delta\omega=0.005$ and calculate the maximal Lyapunov exponent λ_1 for each set of (E_ω,ω). If λ_1 is positive this ω is defined as one of the mappings of E_ω, then the E_ω-ω phase diagram is achieved by depicting all the mappings of each E_ω (the step of E_ω is also set to be 0.005 in the calculations). It is obvious that performing such a calculation of the phase diagram is very time-consuming since we need calculate the maximal Lyapunov exponent λ_1 for each set of (E_ω,ω) to see if $\lambda_1>0$. In Fig. 9, we present the calculated E_ω-ω phase diagram for the GaAs-based quantum dot miniband superlattice of $\Delta=70$ meV at $\alpha=0.0001$ and different lattice temperatures: (a) $T=4.2$, (b) 77, and (c) 300 K, respectively. Every dot $(E_\omega,\ \omega)$ in the figures stands for a chaotic solution. From Fig. 9 we can see an obvious effect of the lattice temperature T on the size of the chaotic region when T is varied from $T=4.2$ to 300 K. With the lattice temperature increasing, the chaotic region becomes smaller and the qualitative change of the pattern constructions is also observed. The most striking qualitative feature shown in Fig. 9 is the clear distinction between the left down boundary of the chaotic region, which appears sharply defined, and the upper boundary, which is substantially more diffuse.

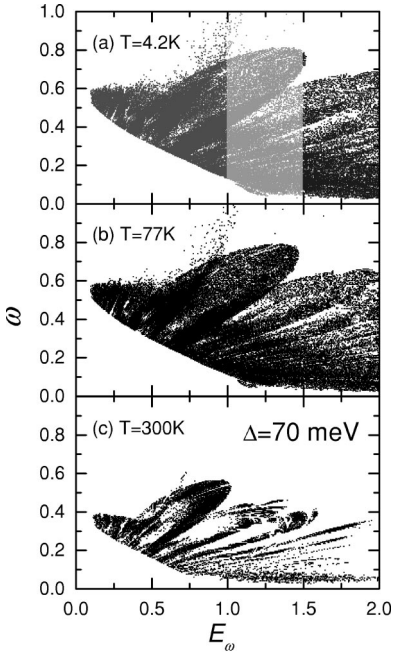

FIG. 9. Calculated E_ω-ω phase diagrams for the quantum dot miniband superlattice of $\Delta=70$ meV at $\alpha=0.0001$ and different lattice temperatures: (a) $T=4.2$, (b) 77, and (c) 300 K, respectively.

As reported by Ref. 4, we have also found from the calculations that many of the positive maximal Lyapunov exponents are nearly zero, thus they are sensitive to small effects of the numerics used. It is therefore difficult to be certain of the boundaries between periodic and chaotic behavior. To illustrate the sensitivity to a cutoff on the size of the maximal Lyapunov exponent λ_1, we have sorted the chaotic regions by λ_1 and shown in Fig. 10 the sorted phase diagrams by setting: (a) $\lambda_1>0.01$, (b) $\lambda_1>0.03$, (c) $\lambda_1>0.04$, and (d) $\lambda_1>0.05$ for the superlattice described in Fig. 9(b). With the controlling value of λ_1 increasing, the size of the chaotic region decreases successively, and the periodic channels become apparent. The presence of these periodic channels within the chaotic region raises the possibility of observing not only chaos in superlattice but also mode locking to various subharmonics of the driving frequency. However, in

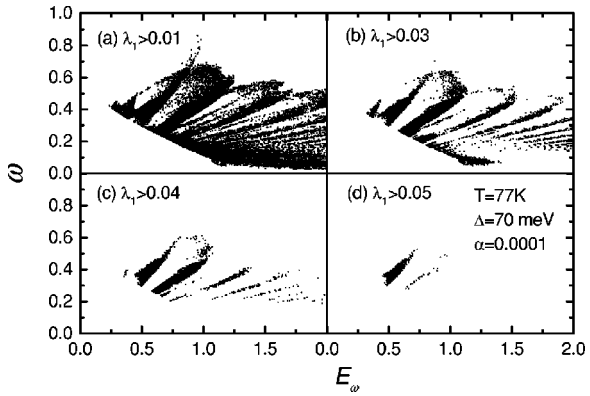

FIG. 10. Phase diagrams with different cutoff values of the maximal Lyapunov exponent λ_1: (a) $\lambda_1>0.01$, (b) $\lambda_1>0.03$, (c) $\lambda_1>0.04$, and (d) $\lambda_1>0.05$, for the quantum-dot miniband superlattice described in Fig. 9(b).

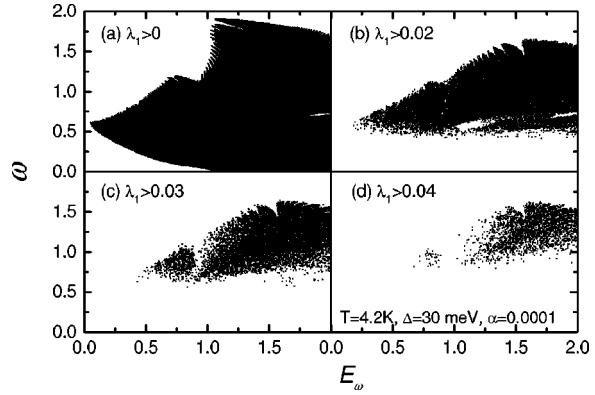

FIG. 11. Phase diagrams with different cutoff values of the maximal Lyapunov exponent λ_1: (a) $\lambda_1>0$, (b) $\lambda_1>0.02$, (c) $\lambda_1>0.03$, and (d) $\lambda_1>0.04$, for the quantum-dot superlattice of $\Delta=30$ meV at $T=4.2$ K and $\alpha=0.0001$.

some cases we have found no an apparent periodic channel within the chaotic regions, as shown in Fig. 11 for the superlattice of $\Delta=30$ meV at $T=4.2$ K and $\alpha=0.0001$. Although the size of the chaotic region decreases with the controlling value of λ_1 increasing from 0 to 0.04, the chaotic regions are always diffuse. The physical origin for the differences of the pattern constructions of the chaotic regions between Figs. 10 and 11 is not clear so far. It may be related to the energy dissipation of the electrons in the minibands. In the latter, the energy-relaxation frequency is smaller than the momentum-relaxation frequency [see Eq. (26)].

It is noted that the adjustable constant α, which describes the relaxation of the self-consistent field and the external circuit, can effect the chaotic behavior of the superlattice system, so we have calculated and shown in Fig. 12 the dependence of the E_ω-ω phase diagrams on the parameter α for the superlattice of $\Delta=70$ meV at $T=300$ K. When varying α from 0.0001 to 0.03 the chaotic regions decrease rapidly. Since α is inversely proportional to the resistance R of the external circuit (see Sec. II), bigger α corresponds to smaller external resistance. We may expect that, for smaller external resistance, the periodic THz radiation encounters a less damping influence of the resistance, thus playing a major role in determining the behavior of the superlattice system and bringing more easily the electron motion into a periodic mode.

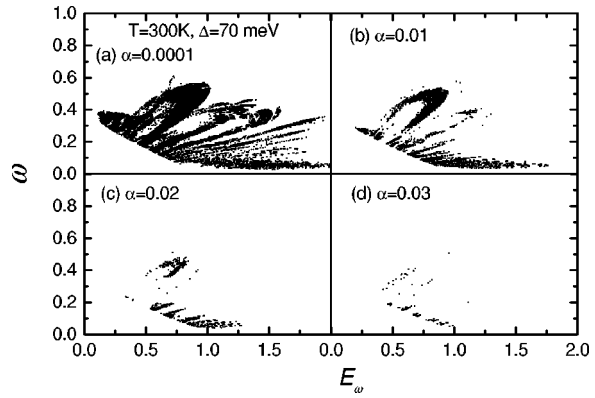

FIG. 12. Calculated E_ω-ω phase diagrams at different α: (a) $\alpha=0.0001$, (b) $\alpha=0.01$, (c) $\alpha=0.02$, and (d) $\alpha=0.03$, for the quantum-dot superlattice of $\Delta=70$ meV at $T=300$ K.

VI. CONCLUSIONS AND REMARKS

On the basis of the time-dependent balance equations for miniband superlattices and the self-consistent field equation, we have extensively investigated the nonlinear dynamical characteristics of the GaAs-based quantum dot miniband superlattices driven by the intense THz radiation field in the form of $E_\omega\cos(\omega\tau)$ at various lattice temperatures, miniband widths, and external circuit conditions. With the controlling parameters E_ω, ω, and α varying in the parameter space, the quantum dot miniband superlattice system is found to exhibit three types of time-dependent behavior: periodic, quasiperiodic, and chaotic. For some parameters the solutions are chaotic and the bifurcation scenarios are very complex. The two-dimensional amplitude-frequency phase diagrams are calculated in order to detect and visualize the chaotic regions in parameter spaces. In the meantime, within the present balance equations we obtain the dependence of chaotic behavior of the superlattice system on superlattice parameters, lattice temperatures, and external circuit conditions, thus providing a possible tool to control chaos. The modulation and elimination of chaos are likely useful in the low-dimensional microstructural devices and in the future nanofabricated semiconductor integrated circuits.

The present paper can be regarded as an extension of Alekseev's phenomenological balance-equation method[4,5] to a more sophisticated physics-based treatment of chaotic dynamics in miniband superlattice, which was proposed as an open question in Ref. 4. The momentum- and energy-balance equation used here are different from those of phenomenological balance-equation method[4,5] in that in the present equations ν_v and ν_ε are derived with a reasonable accuracy from the microscopic frictional acceleration $\tilde{A}$ and energy-transfer rate functions $\tilde{W}$, which are completely determined by and easily calculated from the energy-wave vector dispersion and scattering constants of materials. The microscopic information about energy band structure and scattering process therefore enters into the calculation of the present balance equations in a self-consistent manner. This allows one to realistically treat the scatterings by impurities, acoustic phonons and polar optic-phonons beyond the relaxation-time approximations.[4,5]

We should distinguish the present paper from a recent study by the authors on a N^+NN^+ miniband superlattice device driven by a GHz field,[14] where we investigated field-domain-induced nonlinear dynamics by using the time- and space-dependent hydrodynamic balance equations developed[26,27] for spatially-inhomogeneous semiconductor systems. When the N^+NN^+ superlattice device is subject to a dc bias or dc+ac bias with a GHz frequency, the occurrence of the space charge instability and the formation of electric-field domain make a spatially-inhomogeneous treatment of electron transport quite necessary. In the NDV regime the superlattice can no longer be treated as a spatially homogeneous entity because any small doping/field perturbation can give rise to a large current instability of the entire superlattice system. However, when applying an intense THz electric field to the superlattice, one can sweep through the

NDV regime with a speed faster than the development of the space charge instability and thus avoid the formation of the electric-field domain. In this way, we can therefore explore, with a spatially uniform treatment, the transport characteristics of the superlattice under the influence of an intense THz electric field. Both from the model used in the calculations and from the results obtained, the present investigations on the chaotic dynamics in quantum dot miniband superlattices driven by the THz fields are completely different from those in the N^+NN^+ miniband superlattice devices driven by the GHz fields, which are related to the dynamics of spatiotemporal electric-field domains.[14]

ACKNOWLEDGMENTS

This work was partially supported by the Shanghai Science Foundation for Young Scientists (Qi-Ming Stars) (Grant No. 98QA14002), the National Natural Science Foundation of China (Grant Nos. 69706002 and 19774061), and the Chinese Ministry and Shanghai Municipal Commission of Science and Technology.

[1] L. Esaki and R. Tsu, IBM J. Res. Dev. **14**, 61 (1970).
[2] A. A. Ignatov, E. Schomburg, J. Grenzer, K. F. Renk, and E. P. Dodin, Z. Phys. B: Condens. Matter **98**, 187 (1995).
[3] A. A. Ignatov and A. P. Jauho, J. Appl. Phys. **85**, 3643 (1999).
[4] K. N. Alekseev, G. P. Berman, D. K. Campbell, E. H. Cannon, and M. C. Cargo, Phys. Rev. B **54**, 10 625 (1996).
[5] K. N. Alekseev, E. H. Cannon, J. C. McKinney, F. V. Kusmartsev, and D. K. Campbell, Phys. Rev. Lett. **80**, 2669 (1998).
[6] B. J. Keay, S. J. Allen, Jr., J. Galán, J. P. Kaminski, K. L. Campman, A. C. Gossard, U. Bhattacharya, and M. J. W. Rodwell, Phys. Rev. Lett. **75**, 4098 (1995).
[7] B. J. Keay, S. Zeuner, S. J. Allen, Jr., K. D. Maranowski, A. C. Gossard, U. Bhattacharya, and M. J. W. Rodwell, Phys. Rev. Lett. **75**, 4102 (1995).
[8] K. Unterrainer, B. J. Keay, M. C. Wanke, S. J. Allen, D. Leonard, G. Medeiros-Ribeiro, U. Bhattacharya, and M. J. W. Rodwell, Phys. Rev. Lett. **76**, 2973 (1996).
[9] S. Winnerl, E. Schomburg, J. Grenzer, H.-J. Regl, A. A. Ignatov, K. F. Renk, D. P. Pavel'ev, Yu. Koschurinov, B. Melzer, V. Ustinov, S. Ivanov, S. Schaposchnikov, and P. S. Kop'ev, Superlattices Microstruct. **21**, 91 (1997).
[10] M. C. Wanke, S. J. Allen, K. Maranowski, G. Medeiros-Ribeiro, A. Gossard, and P. Petroff, in *Proceedings of the 23rd International Conference on the Physics of Semiconductors, Berlin, Germany, 1996*, edited by M. Scheffler and R. Zimmermann (World Scientific, Singapore, 1997), p. 1791.
[11] X. L. Lei, J. Appl. Phys. **82**, 718 (1997).
[12] E. Schomburg, A. A. Ignatov, J. Grenzer, K. F. Renk, D. G. Pavel'ev, Yu. Koschurinov, B. Ja. Melzer, S. Ivanov, S. Schaposchnikov, and P. S. Kop'ev, Appl. Phys. Lett. **68**, 1096 (1996).
[13] E. Schomburg, T. Blomeier, K. Hofbeck, J. Grenzer, S. Brandl, I. Lingott, A. A. Ignatov, K. F. Renk, D. G. Pavel'ev, YU. Koschurinov, B. Ya. Melzer, V. M. Ustinov, S. V. Ivanov, A. Zhukov, and P. S. Kop'ev, Phys. Rev. B **58**, 4035 (1998).
[14] J. C. Cao and X. L. Lei, Phys. Rev. B **60**, 1871 (1999).
[15] J. C. Cao and X. L. Lei, Phys. Rev. B **59**, 2119 (1999).
[16] O. M. Bulashenko and L. L. Bonilla, Phys. Rev. B **52**, 7849 (1995).
[17] O. M. Bulashenko, M. J. García, and L. L. Bonilla, Phys. Rev. B **53**, 10 008 (1996).
[18] Y. H. Zhang, J. Kastrup, R. Klann, K. H. Ploog, and H. T. Grahn, Phys. Rev. Lett. **77**, 3001 (1996).
[19] K. J. Luo, H. T. Grahn, K. H. Ploog, and L. L. Bonilla, Phys. Rev. Lett. **81**, 1290 (1998).
[20] K. J. Luo, H. T. Grahn, and K. H. Ploog, Phys. Rev. B **57**, R6838 (1998).
[21] X. L. Lei, N. J. M. Horing, and H. L. Cui, Phys. Rev. Lett. **66**, 3277 (1991).
[22] X. L. Lei, N. J. M. Horing, and H. L. Cui, J. Phys.: Condens. Matter **4**, 9375 (1992).
[23] X. L. Lei, J. Phys.: Condens. Matter **5**, L43 (1993).
[24] E. Ott, *Chaos in Dynamical Systems* (Cambridge University Press, Cambridge, 1993).
[25] A. Wolf, J. B. Swift, H. L. Swinney, and J. A. Vastano, Physica D **16**, 285 (1985).
[26] X. L. Lei, J. Cai, and L. M. Xie, Phys. Rev. B **38**, 1529 (1988).
[27] X. L. Lei, Phys. Status Solidi B **192**, K1 (1995).